Synthesis of single-walled carbon nanotubes in rich hydrogen/air flames

Cen Zhang[a,e,*], Bo Tian[a,d], Cheng Tung Chong[b], Boning Ding[c], Luming Fan[a], Xin Chang[a], Simone Hochgreb[a]

[a] *Department of Engineering, University of Cambridge, Cambridge CB2 1PZ, United Kingdom*
[b] *China-UK Low Carbon College, Shanghai Jiao Tong University, No. 3 Yinlian Rd, Pudong New District, Shanghai 201306, China*
[c] *Department of Materials Science and Metallurgy, University of Cambridge, 27 Charles Babbage Road, Cambridge CB3 0FS, United Kingdom*
[d] *College of Engineering and Technology, University of Derby, Markeaton Street, Derby DE22 3AW, United Kingdom*
[e] *CNOOC Energy Technology & Services Limited, Department of New Energy Technology, No. 6 Dongzhimenwai Xiaojie, Dongcheng District, Beijing 100027, China*

Abstract

We explore the production of single-walled carbon nanotubes (CNTs) in a stream surrounded by rich premixed laminar H_2/air flames using a feedstock containing ethanol and ferrocene. The as-produced nanomaterials were characterised by Raman spectroscopy, transmission electron microscopy, scanning electron microscopy and X-ray diffraction. A formation window of equivalence ratios of 1.00–1.20 was identified, and single-walled CNT bundles with individual CNTs of an average diameter of 1 nm were observed. The formation of CNTs was accompanied by the production of highly crystalline Fe_3O_4 nanoparticles of a size of 20–100 nm. The investigation of the limiting factors for the CNT synthesis was carried out systematically, assisted by numerical

*Corresponding author.
Email address: cz299@alumni.cam.ac.uk (Cen Zhang)

modeling. We conclude that the key factors affecting CNT synthesis are the surrounding flame temperatures, and the concentration of carbon available for CNT nucleation.

---

1. Introduction

Carbon nanotubes (CNTs) were first discovered by Iijima in 1991 whilst using an arc discharge evaporation method for producing fullerene [1]. These hollow-shaped CNTs possess exceptional mechanical, thermal and electrical properties, and therefore are regarded as an advanced functional material. The current mainstream methods for producing CNTs are plasma arc discharge (PAD), pulsed laser vaporisation (PLV) and chemical vapour deposition (CVD). The first two methods are common ways for producing highly crystalline CNTs on a limited scale, while CVD methods are popular tools for mass production of CNTs among which floating catalyst CVD or FCCVD has attracted increasing attention by many researchers and industry due to its continuous, scalable and controllable production characteristics. Catalysts and carbon sources are initially vaporised and mixed in this method before driven into the hot reaction zone, which makes it possible to continuously produce CNTs in a large quantity.

Flame-assisted synthesis is a well-known technique for materials production, and responsible for the high throughput of many commercial products such as carbon black, fumed silica and titanium dioxide pigment [2]. The identification of small amounts of CNTs in flames was first reported by Howard *et.al* [3] using premixed hydrocarbon/oxygen flames (C_2H_2, C_2H_4 and C_6H_6) at low pressures. Since then, different flame configurations have

been developed for producing CNTs, and comprehensive reviews are detailed in Ref.[4–6]. Both diffusion flames [7–9] and premixed flames [10–16] have been used for CNT production. Premixed flames offer certain advantages relatively to their diffusion counterparts, in that the flame structure is one-dimensional and well characterised, with fixed equivalence ratios ϕ that determine the product temperature. The characterisation of the synthesis process by numerical analysis is thereby facilitated [17].

During synthesis, catalysts are either supported on a substrate [7, 11, 13, 15, 18] or carried by gas flows [10, 14, 16, 19–21]. The latter has potential for mass production of CNTs in a continuous production process. There exist a few studies investigating the floating method, primarily focusing on low pressure environment. Diener *et al.* [10] tested different fuels (C_2H_2, C_2H_4 and C_6H_6) and catalyst metallocenes (Fe, Ni and Co) for CNT synthesis at 10 kPa, and reported that C_2H_2 and C_2H_4 were more favoured for high quality CNT production than C_6H_6. Height *et al.* [14] and Wen *et al.* [21] both investigated CNT synthesis on the same setup but using different premixed flames, ($C_2H_2/O_2/15\%Ar$ at 6.7 kPa and $CH_4/O_2/15\%Ar$ at 26 kPa, respectively). By switching the catalyst to iron pentacarbonyl ($Fe(CO)_5$), they both observed the formation of single-walled carbon nanotubes (SWCNTs) accompanying with iron oxide (Fe_3O_4 and Fe_2O_3), and elemental iron nanoparticles; the latter was identified as the direct catalyst for the growth of CNTs. Vander Wal *et al.* created a configuration where the synthesis takes place via pyrolysis instead of complete combustion [19, 20]. This setup consists of a porous premixed burner, with a short central tube carrying the reactants just over the outer flame height, surrounded by a longer, slightly larger metal tube

which serves to contain products and stabilise the diffusion flame. Ferrocene carried by different gas mixtures, $CO/H_2/He$ or $C_2H_2/H_2/He$, was injected through the central tube, while C_2H_2/air premixed flames were stabilised on the burner plate surrounding the tube for heat generation. They found CO was more effective than C_2H_2 as the carbon source, as the latter promotes the formation of polycyclic aromatic hydrocarbons (PAHs) rather than CNTs. Moreover, H_2 were found to be likely to remove excess carbon coating on catalyst nanoparticles and help retain the activity of the catalytic sites for CNT growth [20]. Most recently, a flame-assisted chemical vapor deposition (CVD) method was proposed by Okada *et al* [16]. In this work, a premixed, slightly stoichiometric central Bunsen flame of diluted ethylene and oxygen is used to feed both reactants (ferrocene, sulfur) and fuel (which burn across the flame), whereas further reactants (ethylene, methane, ferrocene, sulfur and are also fed from the outside in the initially cold co-stream. The mixture is then heated with an external furnace to 900–1050 °C. High quality SWCNTs of an average diameter of 0.96 nm and a high carbon purity of 90 wt% were produced using a premixed $C_2H_4/O_2/Ar$ flame at ϕ of 1.05 with ferrocene and sulphur vapour as the catalysts and a furnace heated at 900–1070 ∘C downstream. They discovered that only a small fraction of Fe remained active in growing SWCNTs, and further improvement was needed to the process. In the system described, the reactants undergo a complex temperature and mixture pattern is created, creating a temperature-composition history would be difficult to analyse clearly.

In the present work, we consider a diffusive reactant configuration embedded in a surrounding flow of high temperature gases, in which the dominant

factor is the diffusion of heat and species across the mixing layer surrounding the reactant inlet. Further, our study has a clear advantage that no external furnace is required. This allows both for fast and direct heating of the reactants, and creates a simple system for analysis and modeling, which will eventually help the understanding of the processes involved. Whereas this is not included in the present study, the configuration also allows for eventual optical diagnostics study of these processes, which is not possible in a furnace. These factors are highlighted in the revised text at the end of the introduction section.

We report the formation of highly crystalline SWCNTs of a diameter less than 1 nm, and identify the role of flame product temperature via stoichiometry, and the rate of feedstock and carrier flow rates on the Raman properties and composition of the CNT material.

2. Experimental

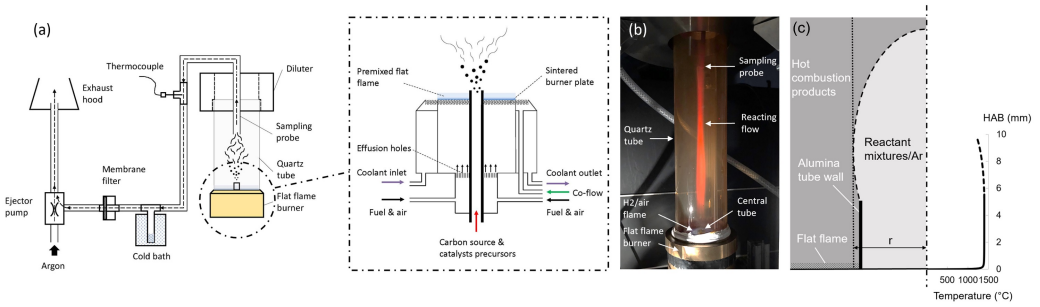

Figure 1: Schematic of the experimental setup. (a) Graphical illustration of the floating catalyst carbon nanotube synthesis apparatus. (b) Image of the reacting environment. (c) Illustration of expected structure of the reaction region and temperature profile at a random radius, r, over different height above burner (HAB) up to 10 mm.

The apparatus consists of a premixed flat flame burner, a flow supply system, and a sampling unit, as depicted in Fig. 1. Premixed H_2/air flames were stabilised on a sintered copper ring (outer diameter 50 mm). An alumina tube (Almath Crucibles Ltd., recrystallised alumina 99.7% purity) of 10 mm outer diameter and 6 mm inner diameter was installed at the centre of the ring for injecting vaporised ethanol (carbon source) and ferrocene (iron precursor). The tube outlet was purposely placed 5 mm above the burner surface to prevent burnout of carbon sources and catalysts by flames. The reacting environment was enclosed by a clear fused quartz tube of 75 mm outer and 70 mm inner diameter (Robson Scientific, SiO_2 99.995%). All flames were operated at atmospheric pressure.

In order to avoid excessive oxidation of the carbon source and catalyst precursors, operating conditions were constrained to rich premixed regions where $\phi \geq 1.00$, from 1.00–1.50. A small amount of CH_4 (0.4 vol.%) was doped for helping visualise the hydrogen flame front as a safety precaution. The contribution of CH_4 to the calculations of ϕ of the flammable mixtures was taken into account.

The experiments initially used the proportions of ethanol and ferrocene that have been successfully applied in FCCVD processes [22–26]. The liquid feedstocks were injected by a syringe pump (World Precision Instruments) at a range of injection rates into a purpose-built atomiser. A stream of argon was fed into the atomiser to carry the atomised feedstock into a temperature-controlled heated pipeline before entering the alumina tube for the subsequent synthesis. The atomiser and the pipeline were heated and maintained at 100 °C to ensure the liquid feedstocks could be fully vaporised. Ethanol

(boiling temperature at 78.37 °C), thiophene (boiling temperature at 84 °C) and ferrocene (sublimation temperature $\geq$ 100 °C) were fully vaporised. The temperature of the vaporised feedstock and the carrier gas were *in situ* monitored by a thermocouple inserted inside the pipeline, just below the bottom of the burner, to ensure a full vaporisation of the injected feedstock.

The baseline feedstock used for the synthesis consisted of 99 wt.% ethanol and 1 wt.% ferrocene. If not explicitly stated otherwise, the feedstock injection rate and the flow rate of the argon flow used for carrying the vaporised reactants were set to 0.5 ml/min and 0.10 slpm, respectively. Accordingly, the mass flow rate of the gaseous feedstocks emerging from the central tube was 0.01 g/s, corresponding to a velocity of 0.27 m/s at the exit of the central tube given at a temperature of 100 °C. To achieve a precise regulation of all gas flows and catalysts, mass flow controllers (Alicat Scientific) were used in the system. Ethanol was chosen as the carbon source and the solvent for dissolving ferrocene. N_2 was for diluting the post-flame products before discharging to the exhaust.

The synthesised materials were collected via a stainless steel probe (6 mm outer and 3 mm inner diameter) positioned at a height above burner (HAB) of 230 mm onto a PTFE membrane filter (SKC Ltd, pore size 0.45 μm). PTFE filters are chemically inert and hydrophobic, and therefore ideal for aerosol sampling in moisture-rich environments. The sampling flows were driven by an ejector pump (SMC ZH05L-X267) and further discharged to an exhaust. A cold finger device was designed to remove water vapour formed during the synthesis. This device consists of a tee pipe fitting with one port connected with a long stainless steel tube inserted into a cold bath filled with

ice. This creates a localised cold spot, which helps effectively condense and reduce water vapour from the sampling flow.

The as-produced samples collected on the PTFE filters were directly analysed by Raman spectroscopy (Horiba XploRA PLUS) in the range of 50–3000 cm^{-1} using a 532 nm wavelength laser. If not explicitly stated otherwise, three separate measurements were carried out on each sample at random locations, covering a region with a diameter of roughly 1.2 μm each. The obtained Raman spectra were then normalised against their respective global peak value before an averaged Raman spectrum for each sample was produced. The nanomaterials were further analysed by X-ray diffraction (Empyrean, Cu anode), scanning electron microscopy (Zeiss Leo Gemini 1530VP FEG-SEM) and transmission electron microscopy (FEI Tecnai Osiris FEGTEM).

3. Estimated product temperatures

The expected temperatures of the 1-D burner stabilised H_2/air flame were simulated using Cantera software [27]. The flame is assumed to be stabilised on a burner surface via heat transfer to the burner by conduction. The equations for mass, energy and species, along with the ideal gas state equation and chemical kinetic rates for the fuels used are solved. The resulting temperature is a function of the the boundary conditions provided by the mass flow rate, mixture composition and temperature of reactants. Details of the solution method are described in Ref.[27, 28].

Figure 2 shows the variation of calculated adiabatic (T_a) and burner stabilised (T_b) flame temperatures and mass fluxes ($\dot{m}''$) of the premixed H_2/air mixtures over equivalence ratios from 1.00 to 1.50. The adiabatic tempera-

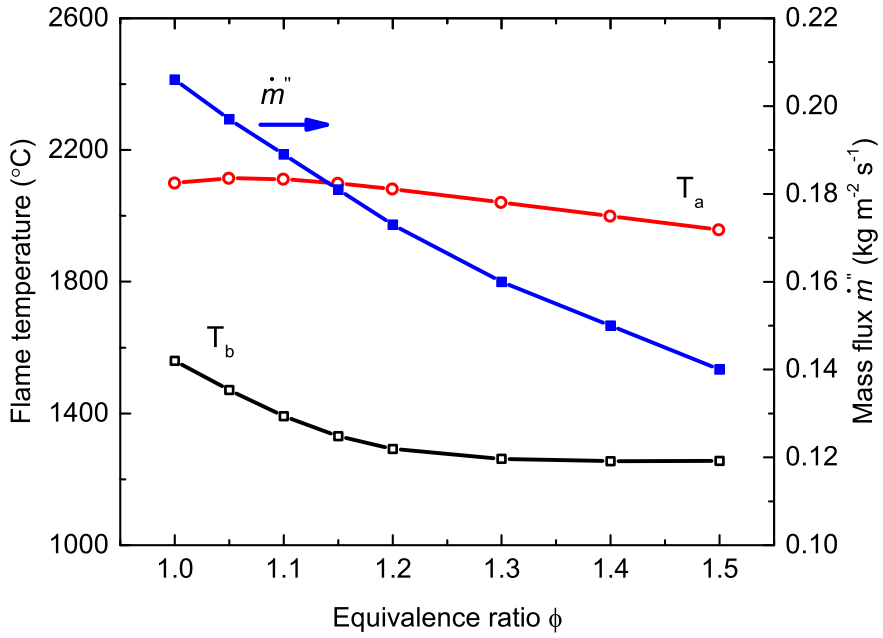

Figure 2: Calculated adiabatic (T_a) and burner stabilised (T_b) flame temperatures and mass fluxes ($\dot{m}''$) of the premixed H_2/air mixtures as a function of equivalence ratios (ϕ). T_b were calculated based on a constant burner temperature of 25 °C and at atmospheric pressure.

ture, T_a, peaks at ϕ=1.05, as determined by the maximum energy release per unit heat capacity of the equilibrium mixture. In contrast, the expected temperature above the burner, T_b, monotonically decreases from 1580 °C with increasing ϕ and reaches a plateau at around 1300 °C when ϕ gets to 1.3. In the present experiment, ϕ was varied by changing the air flow rate while keeping that of H_2 fixed at 7 slpm, which resulted in a decreasing $\dot{m}''$ with increasing ϕ (see Fig.2). Hence, the flame temperature T_b decreases significantly relatively to its adiabatic counterpart, owing to the lower total heat release rate. Lower equivalence ratios were not used, as they were experi-

mentally found to deliver lower CNT yields, as expected from an oxidising environment. No direct measurements of the product gas temperature were made. The 1D models including heat transfer have in the past been shown to give good estimates of the product temperature within 50 K [29].

4. Results and discussion

Figure 1.(b) shows the image of the reacting environment, whereas (c) illustrates the expected structure of the reacting region at the central tube exit and the temperature profile at a random radius, r, over different HABs up to 10 mm. The inner core of the reactants is initially cold, and is heated by diffusive heating by the outer combustion products, leading to a reacting layer at the interface between the cold reactants and the hot water vapour, hydrogen and argon in the flame product gases. The iron-containing compounds react with the OH, O and H radicals in the product gases, leading to Fe_3O_4 formation, which lends the inner column a reddish glow. The length of this column is primarily controlled by the flow rates of the injected feedstock and the argon gases. The elevated high temperatures of this region as a result of heating lead to decomposition of ethanol, forming products of incomplete combustion and small amounts of carbon nanotubes, as shown by the evidence in the following paragraphs.

Figure 3.(a) shows the average normalised Raman spectra of samples produced over different ϕ from 1.00 to 1.50, corresponding to $\dot{m}''$ from 0.21 to 0.14 kg m^2 s^{-1}, and a calculated burnt gas velocity of 1.21 to 1.07 m/s, respectively. Raman features of CNTs, the G-band and a high intensity ratio of the G-band to D-band, I_G/I_D, are clearly seen at ϕ between 1.00

and 1.15. The broad band at 670 cm^{-1} is believed to be a feature peak of magnetite (Fe_3O_4) [30, 31]; while a shoulder alongside this peak at 731 cm^{-1} is attributed to the background signal from the PTFE substrate. As ϕ increases, the CNT Raman features gradually fade away. In contrast, as ϕ approaches the stoichiometric point ($\phi = 1.00$), higher I_G/I_D ratios are achieved, compared with those at richer conditions. This implies a positive relationship between the yield of graphitic CNTs at the highest synthesis temperatures. The results show that the flame temperature is a dominant parameter controlling the synthesis and quality of CNTs. Moreover, there exists an apparent minimum threshold temperature at 1300 °C corresponding to $\phi = 1.20$, above which the Raman signatures of CNTs, the G and D-bands, start to emerge. This finding is in line with the results reported by FCCVD experiments [22, 32, 33], where the formation of SWCNTs and the same Raman signatures start to form beyond 1100 °C.

Figure 3.(b) shows the average normalised Raman spectra of the G-band and D-band of the samples produced at ϕ from 1.00 to 1.15, which are deconvoluted into five Lorentzian peaks in the range of 1000–2000 cm^{-1} using a Gaussian-Lorentzian fitting function, a common algorithm applied for analysing Raman spectra of CNTs [34]. The composite fitting curve, represented by the black thick line, can be fitted in an excellent agreement with the Raman spectra over different ϕ for all cases (($R^2 > 0.98$, where unity indicates a perfect fit). Specifically, the G-band comprises the G^- and G^+ components whereas the D-band comprises the D4, D, and D3 components. Compared with the G-band of graphite, which has only a single Lorentzian peak at 1582 cm^{-1}, the G-band of CNTs, particularly for SWCNTs, typically

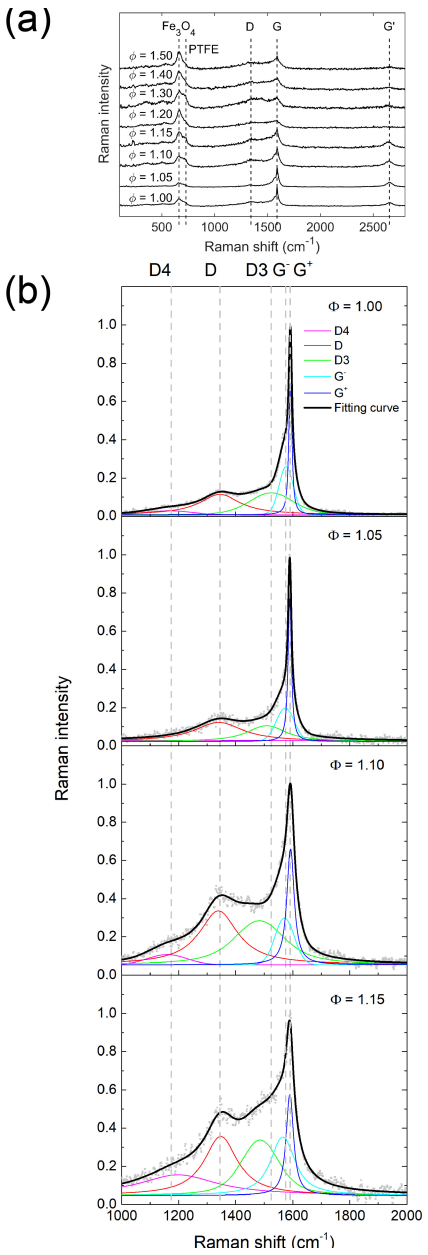

Figure 3: (a) Average normalised Raman spectra of the samples produced at equivalence ratios ϕ from 1.00 to 1.50.(b) Average normalised Raman spectra (shaded dot) and their respective fitted curves (black thick line), along with the spectral deconvolution into Lorentzian peaks in the wavenumber range from 1000 to 2000 cm^{-1} for ϕ from 1.00 to 1.15.

consists of both G^- and G^+ at 1570 cm^{-1} and 1590 cm^{-1}, respectively [35]. The G^+ feature is believed to be associated with the vibrations of carbon atoms in the direction of the axis of a CNT, the G^- feature, on the other hand, is a result of the vibration of carbon atoms along the circumferential direction of a CNT [35]. The Raman spectrum at $\phi = 1.05$ shows the highest G^+ peak (around 0.8) compared with the other conditions, decreasing as ϕ deviates from 1.05. Conversely, the normalised intensity of the G^- peak increases with ϕ deviating from 1.05, resulting in a decreased G^+/G^- intensity ratio. Based on Dresselhaus *et al.*'s theory [35], the relative intensity of G^+/G^- has a marked chirality dependence where semi-conducting CNTs have higher G^+/G^- values while those of metallic CNTs are close to unity . However, this theory was built on the experimental study of isolated SWCNTs rather than bundles, hence, whether the theory still holds remains an open question, and a detailed investigation is needed.

The rise of the D-band of a CNT Raman spectrum is associated with defects or disorder in the materials, and its intensity is mainly a result of the D4, D, and D3 components at around 1200 cm^{-1}, 1340 cm^{-1} and 1500 cm^{-1}, respectively [36]. The exact wavenumbers may deviate depending on the carbon structures of samples and the laser excitation wavelength. The D3 and D4 peaks can only be observed in soot or amorphous carbonaceous materials [36], whereas the D peak is widely seen in many carbon allotropes except for diamond. The rise of the D component, as the most prominent peak in the D-band, is attributed to the vibration of disordered graphitic lattice [36, 37]. On the shoulder this peak, the D4 and D3 peaks are usually observed at lower and higher frequencies, respectively. The former is believed to be a result of the

stretching vibrations of polyene-like structures and ionic impurities [37, 38] while the latter has links with the amorphous contents presenting in soot such as organic molecules and fragments [36, 38]. Generally, the normalised intensity of the D-band comprising all the three featured peaks increases as ϕ departs from 1.05, indicating a inversely proportional relationship with temperature. While that of the D4 peak keeps increasing as ϕ increases, in contrast to the other D peaks, which may indicate an increased proportion of polyene-like structures and ionic impurities formed in the materials.

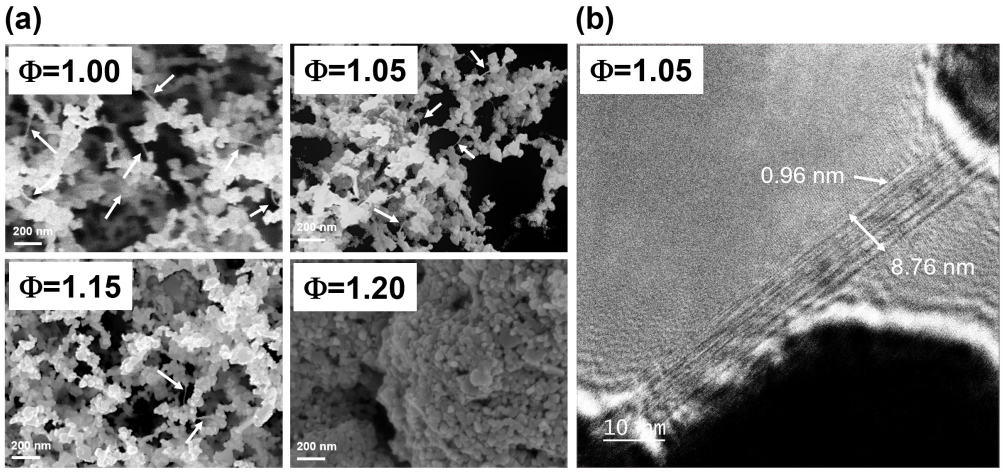

Figure 4: Morphology and structure of the samples produced from the experiments. (a) SEM images of the as-produced nanomaterials at ϕ from 1.00 to 1.20 and (b) TEM image of SWCNTs produced at $\phi = 1.05$.

Figure 4 shows the morphology and structure of nanomaterials synthesised at ϕ from 1.00 to 1.20 using the baseline feedstock. Figure 4.(a) shows that the majority of the collected products consists of crystalline nanoparticles of characteristic size of 20–100 nm. Different shapes of iron oxide nanoparticles are observed, including pyramid, sphere, cube and diamond.

At ϕ=1.00–1.15, CNTs are loosely distributed and attached to the nanoparticles, as indicated by the arrows, tending to form a filamentous or web-like morphology. As ϕ increases to 1.2 and beyond, one starts to observe aggregates or lumps of nanoparticles, exhibiting a different morphology, and very limited quantity of CNTs produced. The TEM image of CNTs products at ϕ of 1.05 (see Fig.4.(b)) suggests that the as-produced CNTs form bundles with a diameter of the order of 10 nm and a length ranging from 100 nm up to 1 μm. Further, the diameter of the constituent individual CNTs was measured to be around 1 nm, implying the CNTs were single-walled.

XRD analysis was applied to investigate the identity of the crystalline nanoparticles. Illustrated in Fig.5 are the XRD patterns of Fe_3O_4, PTFE substrate and the synthesis materials produced at $\phi = 1.05$. The results, together with the featured Raman peak at around 670 cm^{-1} shown in Fig.3.(a), confirms the crystalline nanoparticles consist primarily of Fe_3O_4, to which the CNT fibres are attached.

The mass flux $\dot{m}''$ of the H_2/air mixtures directly affects the synthesis process at a fixed equivalence ratio. Higher mass flux rates lead to higher rates of heat release relatively to the heat loss, leading to higher temperatures (Fig.6.(b)). We investigated this parameter by varying $\dot{m}''$ at a fixed equivalence ratio $\phi = 1.05$.

Test 1 corresponds to a baseline case at $\dot{m}'' = 0.1$ kg m^{-2} s^{-1} (3.5 slpm H_2 and 8.4 slpm air), whereas Test 2–4 were taken at 1.5, 2 and 3 times the mass flow rate of Test 1, respectively. The baseline feedstock was injected at 0.5 ml/min and carried by argon at 0.10 slpm.

Figure 6.(a) shows the normalised Raman spectra of the as-produced sam-

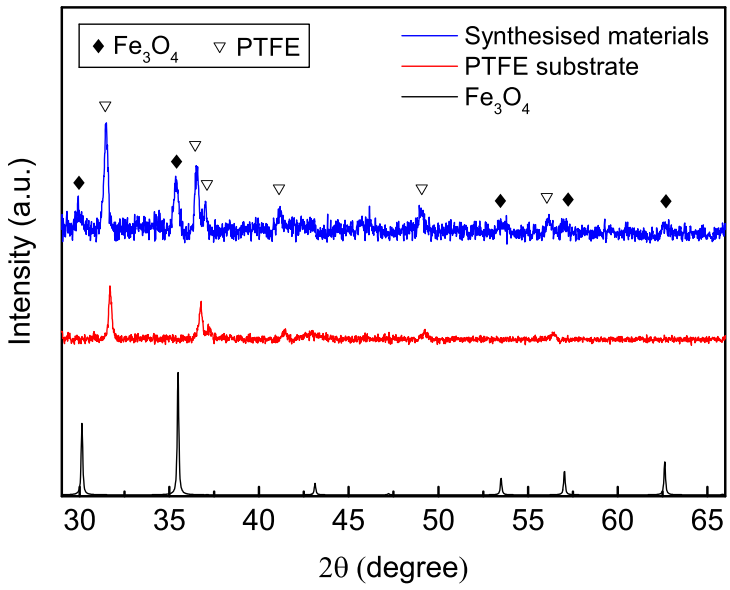

Figure 5: XRD pattern of Fe_3O_4, PTFE substrate and nanomaterials produced at $\phi = 1.05$ using the baseline feedstock.

ples at Test 1–4. The Raman signals become sharper and more distinct with the increase in mass flux $\dot{m}$". For the low mass flux case Test 1, neither the G-band (1590 cm^{-1}) nor the D-band (1350 cm^{-1}) are clearly identified, a sign of low yield of graphitic products. As $\dot{m}$" increases, the featured peak at 731 cm^{-1} originating from the PTFE substrate diminishes, suggesting an increased yield of nanomaterials. It is worth noting that the radial breathing mode (RBM)–a unique Raman signature of CNTs as a result of the coherent radial vibration of C atom at frequencies of 120–350 cm^{-1} [35]–is captured by Raman spectroscopy as shown on the spectra of Test 2–4. Meanwhile, other Raman features of CNTs, the G-band, D-band and G'-band, also arise. Apparently, higher $\dot{m}$" favours the formation of CNTs rather than the opposite,

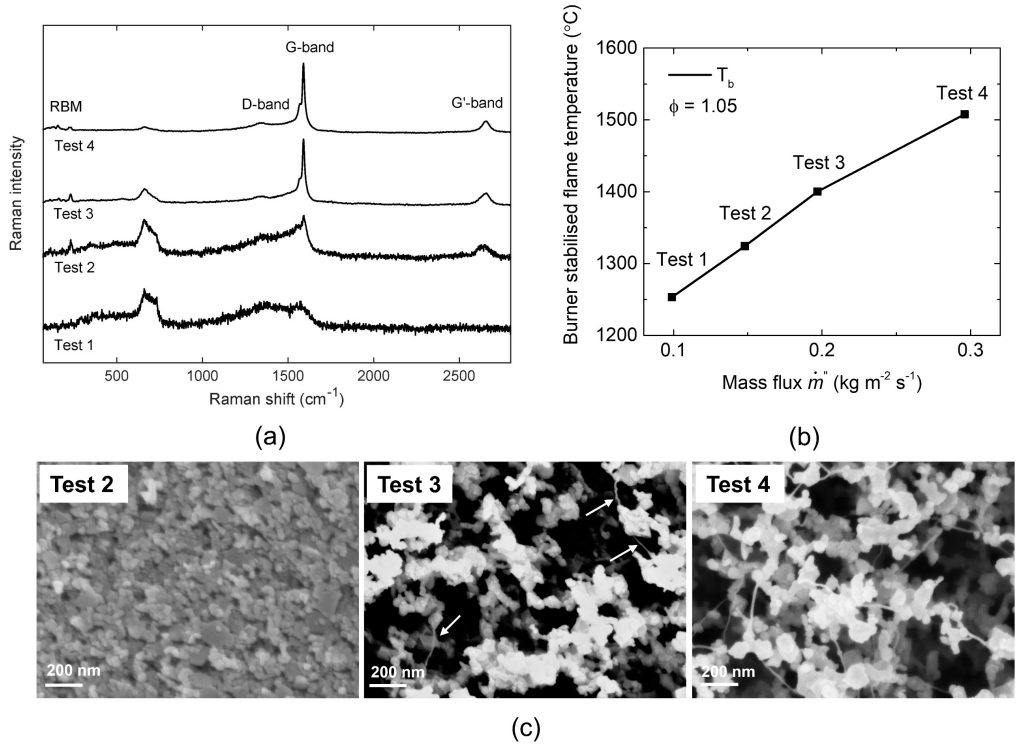

Figure 6: (a) Average normalised Raman spectra of the nanomaterials produced at $\phi = 1.05$ over different $\dot{m}^{"}$ (0.1, 0.15, 0.2, and 0.3 kg m^{-2} s^{-1} corresponding to Tests 1–4, respectively). (b) Variation of calculated burner stabilised flame temperature T_b as a function of $\dot{m}^{''}$ (at atmospheric pressure and at an inlet temperature of 25 °C). (c) SEM images of the nanomaterials collected at Test 2–4. Arrows indicate location of filamentous CNT.

and it is evidenced by the drastic elevation of the I_G/I_D ratio which increases from 0.98 to 10.0 as $\dot{m}^{"}$ changes from 0.1 to 0.3 kg m^{-2} s^{-1}. Again, the calculated T_b suggests that the threshold temperature for CNT formation is around 1300 °C, which agrees with the findings highlighted in Fig. 2.

A detailed examination of the material morphologies for different $\dot{m}^{"}$ from Test 2 to 4 was conducted by SEM as shown in Fig.6.(c). The figure illustrates the evolution of morphology of the nanomaterials as $\dot{m}^{"}$ increases. The morphology for Test 1 is very similar to that of Test 2, and is therefore not included in the figure. For Test 2, only densely-packed solid nanoparticles were observed by SEM rather than CNTs, although some CNT fibres might be embedded beneath the nanoparticles as indicated by the Raman spectrum. As the mass fluxes (and the corresponding temperatures) increased, CNTs formed a filamentous framework with crystalline nanoparticles attached (Fig.4). This type of arrangement implies an increased yield of CNTs, and an enhanced number density of CNTs to nanoparticles. More specifically, CNTs are more easily observed in Test 4 than any other conditions, due to a larger quantity and longer lengths of the CNT materials.

4.1. Effect of reactant injection rates

The rate of injection of the centrally injected reactants, $\dot{q}$, and the carrier gas flow rate, $\dot{v}_{Ar}$, were investigated in the following experiments.

The background product conditions of the were fixed at $\phi = 1.05$ (7 slpm H_2 and 16.7 slpm air), which yielded a calculated synthesis temperature of 1450 °C, leading to an expected product gas velocity u_b of 57.3 cm/s. The effect of $\dot{v}_{Ar}$ was first examined by varying its value from 0.05 to 1.00 slpm, whilst keeping $\dot{q}$ fixed at 0.5 ml/min. Figure 7.(a) shows the average

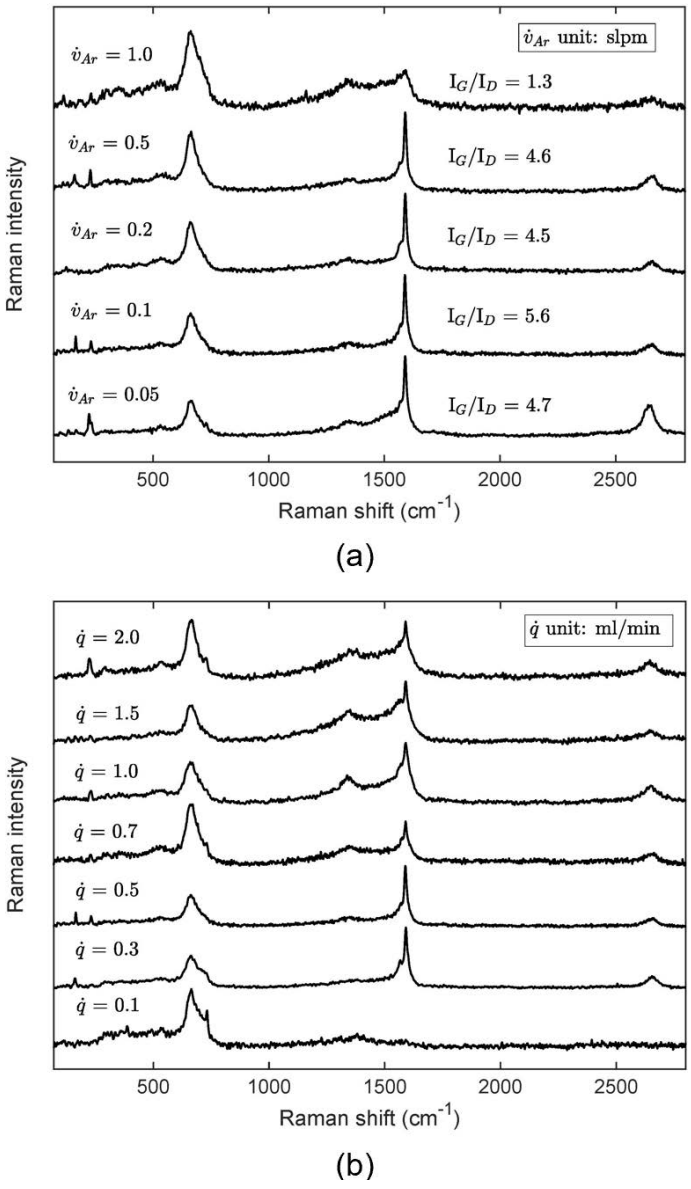

Figure 7: Average normalised Raman spectra of the samples produced at $\phi = 1.05$ as a function of (a) different injection rates $\dot{q}$ from 0.1 to 2.0 ml/min, and (b) different argon flow rates $\dot{v}_{Ar}$ from 0.05 to 1.00 slpm.

normalised Raman spectra of nanomaterials synthesised at different $\dot{v}_{Ar}$. In general, the variation of $\dot{v}_{Ar}$ shows little effect on the CNT synthesis up to 0.50 slpm, corresponding to a flow velocity of 64.0 cm/s comparable to that of the surrounding burnt gas flow of 57.3 cm/s. These Raman spectra exhibit a similar pattern as the Raman features of CNTs previously observed near the stoichiometric ratio, and the associated I_G/I_D ratios are all at around 5.0, suggesting a production of high quality CNTs. In contrast, when $\dot{v}_{Ar}$ reaches 1.00 slpm, at an estimated flow velocity equivalent to twice the value of the surrounding hot gases, the synthesised materials show a much poorer Raman spectra, indicating a decreased yield of CNTs and an increased proportion of amorphous carbon solids. This behaviour shows that for low values of the central gas velocity, the CNT formation is controlled by the diffusion of heat, and corresponding reaction between the central reactants, heated by the surrounding gases. Beyond a certain inlet flow rate, however, heat diffusion through the reactant layer is insufficiently fast, and the inner reactant core leaves the system unreacted.

The reactant injection rate $\dot{q}$ was varied from 0.1 to 2.0 ml/min for a constant carrier flow rate $\dot{v}_{Ar}$ of 0.10 slpm, thus increasing the concentration of reactants by a factor of 20. The average normalised Raman spectra of the nanomaterials produced are shown in Fig.7.(b). Generally, the G-band and the RBM can be observed for all $\dot{q}$, except for the lowest flow rates of 0.1 ml/min where no Raman features of CNTs are discerned, for which only Fe_3O_4 nanoparticles are detected by Raman spectroscopy, as the concentration of carbon source precursors are too low. As $\dot{q}$ increases beyond 0.1 ml/min, it is found that an optimum condition is reached, at which the Ra-

man spectrum exhibits the most distinct features for $\dot{q}$ from 0.3 to 0.5 ml/min. Beyond 0.5 ml/min, the Raman spectra exhibit a broadened G-band and an enhanced D-band for all the conditions considered. The broadening effect appears due to the rise of the D3 peak, which is linked with amorphous species such as organic molecules or fragments [36, 38] as discussed in the previous section. A drop in I_G/I_D ratios signals a decreased yield of CNTs for higher $\dot{q}$. The behaviour suggests that there is a minimum reactant concentration for the formation of CNTs, and that at some critical concentration, it is no longer the limiting factor for their formation. Beyond a certain concentration, the rate of heat diffusion into the central reactant column becomes rate limiting, so that higher concentrations just lead to poorer quality CNTs, and conversion into alternative products.

5. Conclusions

In this study, we have successfully demonstrated the potential of using a H_2/air background premixed flame to continuously produce CNTs using ethanol, ferrocene and thiophene. In contrast with previous premixed flame syntheses processes, the present study uses (close to) zero carbon in the surrounding hot product gas atmosphere, thus simplifying the arrangement and allowing for a greater understanding of how CNTs form in the mixing layer. Compared to a furnace environment, the hydrogen flame-surrounded environment offers fast heating and reacting environment relatively to the slow heating environment of a furnace. On the other hand, the remaining oxygen bound to OH and water does create an opportunity for oxidation, which means that the environment is best suited for situations where an

oxide bound with CNTs is desirable. Specific findings are are as follows:

- The temperature and stoichiometry of the surrounding product gases are key to successful CNT synthesis; operating at equivalence ratios just rich of the stoichiometric point leads to the highest Raman signals favourable for producing CNTs, as little oxygen is left in the pyrolysis zone, avoiding rapid oxidation of the catalyst nanoparticles.

- Fe_3O_4 crystals are still abundantly formed, even under conditions of rich products, owing to the high concentrations of OH still available in the hot gases. SWCNTs form as nanometer-thick fibrelets connecting the surrounding Fe_3O_4 crystals.

- Higher mass fluxes of the surrounding burnt gases lead to higher heat release per unit heat loss, and thus higher temperatures. This contributes to higher quantities, length and quality of CNTs formed.

- There is an optimal range of both carrier flow rate and reactant concentration which maximises the quantity and quality of CNTs sampled. The results seem to indicate that there the limiting factor is the rate of diffusive heating of the reactants by the surrounding gases: beyond a limiting reactant gas or concentration flow rate, the heat cannot be transferred fast enough, and the CNT product quantity and quality degrades.

The present method is promising and inexpensive means of for CNT generation, particularly if the catalyst is chosen to be a desirable part of the product, for example oxide particles connected to CNTs for electrodes. How-

ever, significant work is required to better quantify the product yield in the present process.

Acknowledgements

Cen Zhang thanks the China Scholarship Council and the Cambridge Trust for the financial support towards this research work. The overall project is funded under EPSRC UK Award EP/M015211/1 for the ANAM Initiative. The authors thank Dr Xiao Zhang and Dr Yanting Jin for their help with Raman and XRD analysis. The authors are also grateful to Dr Adam Boies and Prof Alan Windle for helpful discussions.

References

[1] S. Iijima, nature 354 (1991) 56–58.

[2] W. Y. Teoh, R. Amal, L. Mädler, Nanoscale 2 (2010) 1324–1347.

[3] J. Howard, K. Chowdhury, J. Sande, Nature 370 (1994) 603.

[4] W. Merchan-Merchan, A. V. Saveliev, L. Kennedy, W. C. Jimenez, Progress in Energy and Combustion Science 36 (2010) 696–727.

[5] S. Li, Y. Ren, P. Biswas, S. D. Tse, Progress in Energy and Combustion Science 55 (2016) 1–59.

[6] N. Hamzah, M. F. Yasin, M. Z. Yusop, A. Saat, N. A. Subha, Journal of Materials Chemistry A 5 (2017) 25144–25170.

[7] R. L. Vander Wal, L. J. Hall, G. M. Berger, The Journal of Physical Chemistry B 106 (2002) 13122–13132.

[8] L. Yuan, K. Saito, C. Pan, F. Williams, A. Gordon, Chemical Physics Letters 340 (2001) 237–241.

[9] W. Merchan-Merchan, A. Saveliev, Chemical Physics Letters 354 (2002) 20–24.

[10] M. D. Diener, N. Nichelson, J. M. Alford, The Journal of Physical Chemistry B 104 (2000) 9615–9620.

[11] R. L. Vander Wal, L. J. Hall, G. M. Berger, Proceedings of the Combustion Institute 29 (2002) 1079–1085.

[12] R. V. Wal, L. Hall, Chemical Physics Letters 349 (2001) 178–184.

[13] R. Vander Wal, Carbon 40 (2002) 2101–2107.

[14] M. J. Height, J. B. Howard, J. W. Tester, J. B. Vander Sande, Carbon 42 (2004) 2295–2307.

[15] C. T. Chong, W. H. Tan, S. L. Lee, W. W. F. Chong, S. S. Lam, A. Valera-Medina, Materials Chemistry and Physics 197 (2017) 246–255.

[16] S. Okada, H. Sugime, K. Hasegawa, T. Osawa, S. Kataoka, H. Sugiura, S. Noda, Carbon 138 (2018) 1–7.

[17] G. Mittal, V. Dhand, K. Y. Rhee, H.-J. Kim, D. H. Jung, Carbon Letters 16 (2015) 1–10.

[18] P. Gopinath, J. Gore, Combustion and Flame 151 (2007) 542–550.

[19] R. L. Vander Wal, L. J. Hall, Combustion and Flame 130 (2002) 27–36.

[20] R. L. Vander Wal, Combustion and Flame 130 (2002) 37–47.

[21] J. Z. Wen, H. Richter, W. H. Green, J. B. Howard, M. Treska, P. M. Jardim, J. B. Vander Sande, Journal of Materials Chemistry 18 (2008) 1561.

[22] Y.-L. Li, I. A. Kinloch, A. H. Windle, Science (New York, N.Y.) 304 (2004) 276–8.

[23] S. Chaisitsak, J. Nukeaw, A. Tuantranont, Diamond and Related Materials 16 (2007) 1958–1966.

[24] Y.-L. Li, L.-H. Zhang, X.-H. Zhong, A. H. Windle, Nanotechnology 18 (2007) 225604.

[25] M. S. Motta, A. Moisala, I. A. Kinloch, A. H. Windle, Journal of Nanoscience and Nanotechnology 8 (2008) 2442–2449.

[26] C. Hoecker, F. Smail, M. Pick, A. Boies, Chemical Engineering Journal 314 (2017) 388–395.

[27] D. G. Goodwin, H. K. Moffat, R. L. Speth, Cantera: An Object-Oriented Software Toolkit For Chemical Kinetics, Thermodynamics, And Transport Processes. Version 2.3.0, 2017.

[28] M. D. Smooke, Journal of Computational Physics 48 (1982) 72–105.

[29] M. A. Gregor, A. Dreizler, Meas. Sci. Technol. (2009) 065402.

[30] L. Slavov, M. V. Abrashev, T. Merodiiska, C. Gelev, R. E. Vandenberghe, I. Markova-Deneva, et al, Journal of Magnetism and Magnetic Materials 322 (2010) 1904–1911.

[31] D. L. A. de Faria, S. Venâncio Silva, M. T. de Oliveira, Journal of Raman Spectroscopy 28 (1997) 873–878.

[32] C. Hoecker, F. Smail, M. Bajada, M. Pick, A. Boies, Carbon 96 (2016) 116–124.

[33] G. Hou, D. Chauhan, V. Ng, C. Xu, Z. Yin, M. Paine, et al, Materials and Design 132 (2017) 112–118.

[34] S. L. H. Rebelo, A. Guedes, M. E. Szefczyk, M. Pereira, C. Freire, Physical Chemistry Chemical Physics 18 (2016) 12784–12796.

[35] M. S. Dresselhaus, G. Dresselhaus, R. Saito, A. Jorio, Physics Reports 409 (2005) 47–99.

[36] A. Sadezky, H. Muckenhuber, H. Grothe, R. Niessner, U. Pöschl, Carbon 43 (2005) 1731–1742.

[37] A. C. Allwood, M. R. Walter, C. P. Marshall, Vibrational Spectroscopy 41 (2006) 190–197.

[38] M. Knauer, M. Carrara, D. Rothe, R. Niessner, N. P. Ivleva, Aerosol Science and Technology 43 (2009) 1–8.